Nanoscale

PAPER

View Article Online
View Journal | View Issue

Check for updates

Cite this: *Nanoscale*, 2025, **17**, 26982

Dye-sensitized upconversion nanoparticles with enhanced aqueous luminescence for neuronal imaging

Hengde Li, [a] Haitao Liu, [a] Ka-Leung Wong, *[b] Mohsen Adeli *[c,d] and Angelo H. All *[a]

The combination of organic dyes as photosensitizers with inorganic upconversion nanoparticles (UCNPs) has significantly enhanced upconversion luminescence when excited with near-infrared (NIR) light. Additionally, by employing surface functionalization techniques, a high signal-to-noise ratio can be achieved, resulting in exceptional resolution for bioimaging. The objective of our study was to develop a heptamethylcyanine derivative (IR61-BF) for dye-sensitized UCNPs, enhancing their luminescence efficiency in aqueous solutions. This was done by introducing a difluorobenzene group into the cyanine structure. Rare earth-doped UCNPs with a core–shell structure, $NaYF_4$:YbTm@$NaYF_4$:YbNd, were synthesized using a high-temperature decomposition method. In this structure, the Nd^{3+} ions function as efficient sensitizers by absorbing 808 nm NIR light. To further enhance the upconversion efficiency, the molecular structure of the NIR dye IR61 was optimized. By integrating a difluorinated phenyl group into the cyanine backbone, we significantly increased the fluorescence quantum yield of the dye and enhanced the dye sensitization effect of the UCNPs. Subsequently, the UCNPs were coated with an amphiphilic ligand, DSPE-PEG, and IR61-BF was incorporated into the hydrophobic region between the UCNPs, and a remarkable 167.1-fold enhancement in upconversion luminescence in the aqueous phase was achieved. Their biocompatibility for neuronal imaging was evaluated using NSC34, Neuro2a, and C6 glioma cells, while their potential for retrograde intra-neuronal delivery was confirmed by using a microfluidic model of cortical neurons. We demonstrated that the newly synthesized heptamethine cyanine derivative IR61-BF shows exceptional sensitization of UCNPs due to the incorporation of a difluorobenzene group, particularly in aqueous solutions.

Received 4th August 2025,
Accepted 29th October 2025

DOI: 10.1039/d5nr03288a

rsc.li/nanoscale

Open Access Article. Published on 29 October 2025. Downloaded on 6/21/2026 12:21:52 PM.
This article is licensed under a Creative Commons Attribution-NonCommercial 3.0 Unported Licence.

1. Introduction

Upconversion nanoparticles (UCNPs) represent an advanced class of nanomaterials capable of converting low-energy near-infrared (NIR) light into high-energy visible light through a nonlinear optical process.[1–3] These nanoparticles are typically composed of rare earth element-doped nanocrystals, including ions such as Yb^{3+}, Er^{3+}, and Tm^{3+}. Their NIR excitation and multi-color visible light emission capabilities effectively address the tissue scattering and autofluorescence commonly associated with traditional optical imaging, resulting in high-resolution imaging,[4–6] and offer distinct advantages in neuroscience research,[7,8] particularly in deep neuron imaging and retrograde tracing.[9,10] However, a notable limitation of UCNPs is their relatively low absorption cross-section in the NIR spectrum, which significantly limits their effectiveness in upconversion processes.[11] To enhance the luminescence efficiency of UCNPs, several methodologies have been explored, among which dye sensitization has emerged as an effective strategy.[12–16] This approach involves the integration of organic dye molecules with UCNPs, effectively leveraging dye molecules to absorb external excitation photons and subsequently transfer the captured energy to the activator ions within the UCNPs through energy transfer, thereby significantly increasing the upconversion luminescence (UCL) efficiency.[17–20]

Cyanine derivatives are widely utilized organic dyes in the dye-sensitized UCNP process due to their high absorption cross-section and broad absorption spectrum.[21–23] During the dye-sensitized UCNP process, the cyanine molecule experiences a non-radiative transition from the ground state to the

[a]*Department of Chemistry, Hong Kong Baptist University, Hong Kong SAR, China. E-mail: angelo@hkbu.edu.hk*
[b]*Department of Applied Biology and Chemical Technology, The Hong Kong Polytechnic University, Hong Kong SAR, China. E-mail: klgwong@polyu.edu.hk*
[c]*Institut für Chemie und Biochemie, Freie Universität Berlin, Berlin, Germany*
[d]*Faculty of Chemistry, Dept. of Organic Chemistry, Lorestan University, Khorramabad, Iran. E-mail: adeli.m@lu.ac.ir*

This journal is © The Royal Society of Chemistry 2025

Open Access Article. Published on 29 October 2025. Downloaded on 6/21/2026 12:21:52 PM.
This article is licensed under a Creative Commons Attribution-NonCommercial 3.0 Unported Licence.

excited state upon absorbing light energy. This absorbed energy is subsequently transferred to the UCNPs.[20] By manipulating various factors, such as the concentration of cyanine molecules and the distance between the UCNPs and cyanine, effective energy transfer can be achieved, thereby enhancing the luminescence efficiency of the UCNPs.[24,25]

Numerous cyanine derivatives have been synthesized and studied for their potential in UCNP sensitization strategies. For instance, 1,3,5,7-cyclotetraenes (COT), known as triplet-state inhibitors, have been integrated into the structure of the cyanine derivative IR806 to mitigate the significant photobleaching phenomenon that commonly occurs in dye-sensitized upconversion systems at room temperature.[26] However, their stability in aerated solutions is often compromised due to the degradation of the COT. To address this issue, a bulky moiety (4-(1,2,2-triphenyl vinyl)-1,1′-biphenyl (TPEO)) is incorporated into IR806, which can effectively inhibit the oxidation of the polymethyl structure by oxygen molecules, thereby stabilizing the properties of NIR dyes.[24] Qian Liu *et al.* reported a novel NIR probe, SQ-739, based on squaraine for dye sensitization in upconversion. When excited at 730 nm, SQ-739 coordination was used to coat Nd-doped UCNPs, which significantly enhanced the UCL emission. In comparison with the commonly used heptamethine cyanine-based IR806, SQ-739-UCNPs exhibit a highly stable UCL emission with no significant aggregation-caused quenching (ACQ), which often limits the brightness of dye sensitization. Additionally, SQ-739 demonstrates excellent chemical and light stability.[27] Furthermore, cyanine dye IR806 sensitized UCNPs show considerable potential for applications in bioimaging, photodynamic therapy (PDT), and cell imaging.[28]

Considering the requirements of neuronal imaging applications, the development of water-soluble UCNP probes is essential for their biomedical applications, directly affecting their biocompatibility, stability, and functionality.[29,30] Although dye-sensitized UCNPs can achieve sensitization hundreds of thousands of times in organic solutions,[24] their sensitization efficiency in the aqueous phase is severely limited.[31] This indicates that the dye-sensitization strategy is still unable to solve the bottleneck problem of UCL light brightness in biological aqueous environments.

Here, we report a core–shell structured UCNP ($NaYF_4$:YbTm@$NaYF_4$:YbNd) that integrates NIR dyes on its surface. The core contains Tm^{3+} activators and the intermediate layer has Nd^{3+} sensitizers, and the effective excitation between them was mediated by Yb^{3+}, resulting in bright blue UCL under 808 nm laser excitation. Modifications to the heptamethine cyanine derivative IR61, including the replacement of chlorine with a difluorobenzene group, result in the creation of IR61-BF, which improves NIR light absorption and enhances the fluorescence quantum yield. Additionally, the side chains of benzoic acid enhance the dye's affinity and improve the energy transfer efficiency to UCNPs. Notably, IR61-BF achieves a remarkable 167.1-fold enhancement in UCL in the aqueous phase. We further demonstrate the outstanding performance of this nanoscale system as a high-precision neuronal imaging probe through *in vitro* cell experiments. By using a primary neuron microfluidic model, we introduce a new tool in the fields of neuroscience and bioimaging.

2. Materials and methods

2.1. Synthesis of UCNPs

Synthesis of $NaYF_4$:YbTm core nanoparticles. A solution containing 1 mmol of lanthanide acetate (comprising 79.5% Y^{3+}, 20% Yb^{3+}, and 0.5% Tm^{3+}) in water was combined with 6 mL of oleic acid (OA) and 15 mL of 1-octadecene (ODE) in a 100 mL two-neck flask. The mixture was then heated to 150 °C under nitrogen flow and maintained at this temperature for 60 minutes to remove water, resulting in a clear and transparent solution. After cooling to room temperature, 100 mg of NaOH and 148 mg of NH_4F in 6 mL of MeOH were added. The reaction mixture was stirred at 50 °C for 30 minutes, then heated to 110 °C and kept for 10 minutes. After degassing for 10 minutes, the mixture was heated to 290 °C for 90 minutes under N_2 protection. After the reaction was complete, the mixture was cooled to room temperature, and then 20 mL of ethanol was added. The core UCNPs were obtained by centrifugation (6000 rpm, 10 min) after ultrasonic mixing. The formed UCNPs were then purified by redispersing them in cyclohexane and precipitating with ethanol three times. Finally, the UCNPs were dispersed and stored in 4 mL of cyclohexane.

Synthesis of $NaYF_4$:YbTm@$NaYF_4$:YbNd core–shell nanoparticles. In a standard procedure, a mixture containing 0.35 mmol of Y^{3+}, 0.05 mmol of Yb^{3+}, and 0.1 mmol of Nd^{3+} was combined with 3 mL of OA and 7 mL of ODE in a 100 mL two-neck flask. The mixture was heated to 150 °C under nitrogen flow and maintained at this temperature for 60 minutes to eliminate water. After cooling to 90 °C, 2 mL of core UCNPs in cyclohexane solution was introduced and kept at this temperature to remove the cyclohexane. Subsequently, the mixture was cooled to room temperature, and 50 mg of NaOH and 74 mg of NH_4F in 3 mL of MeOH were added. The reaction mixture was stirred at 50 °C for 30 minutes, then heated to 110 °C and kept for 10 minutes. After degassing for 10 minutes, the mixture was further heated to 290 °C for 90 minutes under a N_2 atmosphere. After cooling the mixture to room temperature, 20 mL of ethanol was added. The core–shell UCNPs were obtained by centrifugation (6000 rpm, 10 min) after ultrasonic mixing. The UCNPs were then purified by redispersing in cyclohexane and precipitating with ethanol three times. Finally, the core–shell UCNPs were dispersed and stored in cyclohexane.

2.2. UCNP sensitization test

Preparation of $NOBF_4$ coated UCNPs. A solution of UCNP@OA in cyclohexane (10 mL, 5 mg mL^{-1}) was combined with 50 mL of 0.01 mol mL^{-1} $NOBF_4$ in DMF. After stirring for 10 minutes, the top layer of cyclohexane was removed. Subsequently, toluene/cyclohexane (15/15 mL) was added,

Open Access Article. Published on 29 October 2025. Downloaded on 6/21/2026 12:21:52 PM.
This article is licensed under a Creative Commons Attribution-NonCommercial 3.0 Unported Licence.

thoroughly mixed, and then centrifuged at 12 000 rpm for 10 min to obtain UCNP@NOBF$_4$. The UCNP@NOBF$_4$ was stored in DMF at a concentration of 10 mg mL^{-1}.

Preparation of dye-sensitized UCNPs. UCNP@NOBF$_4$ nanoparticles (1 mg L^{-1} final concentration) were mixed with various concentrations of IR61 or IR61-BF (0–10 μM) in DMF. After incubation at room temperature for 30 min, the fluorescence spectrum was obtained using a Horiba FluoroMax-4 (FM-4) Photoluminescence Spectrometer (light source: 808 nm laser or 805 nm LED).

Preparation of UCNP@PEG and UCNP@PEG&IR61-BF. UCNP@OA (1 mg mL^{-1}), DSPE-PEG (1 mg mL^{-1}), and various concentrations of IR61-BF (0–10 μM) in $CHCl_3$ were stirred at room temperature. After removing the solvent under a nitrogen atmosphere, the resulting product was dispersed in ultrapure water, referred to as UCNP@PEG and UCNP@PEG&IR61-BF nanoparticles, respectively. The resulting nanoparticles were subsequently dispersed in ultrapure water at a concentration of 1 mg mL^{-1} and tested using FM-4.

3. Results and discussion

3.1. Synthesis of near infrared dyes

Infrared dyes IR61 and IR61-BF were synthesized using a multi-step method (Scheme 1). First, compound 1 was synthesized by reacting 2,3,3-trimethyl-3*H*-indole with 4-bromomethylbenzoic acid. The introduction of a benzene ring can effectively improve the degree of conjugation of molecules, thus enhancing the efficiency of electron transport. The conjugated system allows the molecules to transfer energy more efficiently during light absorption and emission through the delocalization of π electrons, and the introduction of carboxyl groups improves the solubility of dyes and the anchoring of UCNPs. Then, the compound was further condensed with *N*-((2-chloro-3-((phenylphenyl)methyl)cyclohexyl-2-ene-1-acyl)methyl)aniline hydrochloride, and IR61 was synthesized. Finally, IR61-BF was obtained by a Suzuki reaction with 3,5-difluorophenylboronic acid. The obtained small organic molecules were purified by column chromatography and characterized by ^{1}H NMR, ^{13}C NMR and HRMS (see the SI).

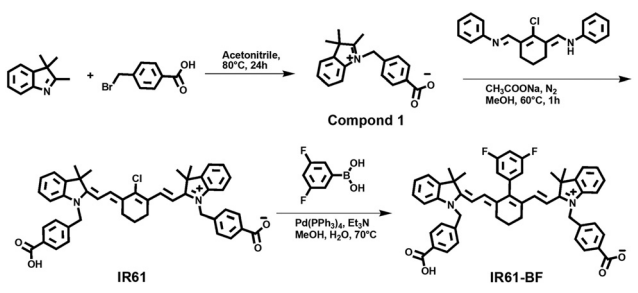

Scheme 1 Synthetic scheme of IR61-BF.

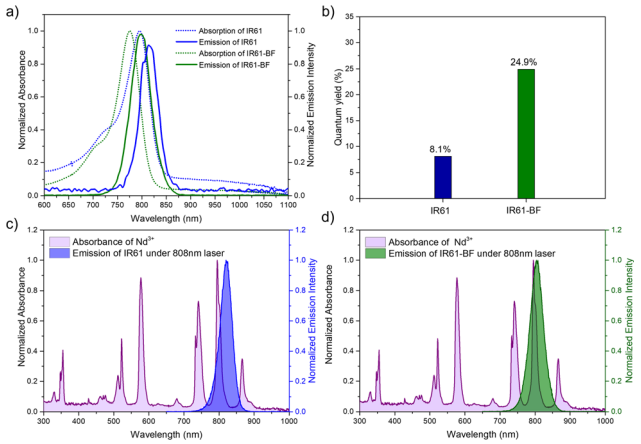

Fig. 1 (a) The normalized absorption and emission spectra of IR61 (λ_{abs} = 797 nm, λ_{em} = 815 nm marked in blue) and IR61-BF (λ_{abs} = 779 nm, λ_{em} = 800 nm marked in green) dyes. (b) The quantum yield of IR61-BF is increased by >3 fold because of the introduction of difluorobenzene groups in IR61. (c) The normalized absorption spectrum of Nd^{3+} and the emission spectrum of IR61. (d) The normalized absorption spectrum of Nd^{3+} and the emission spectrum of IR61-BF, which show better overlap than those of IR61.

The optical properties of the dyes dissolved in DMF were investigated (Fig. 1). The dye IR61 displayed a prominent absorption peak at 797 nm, characterized by a high absorption coefficient of 5.137 × 10^4 M^{-1} cm^{-1}, along with an emission peak at 815 nm. In comparison with IR61, the modification incorporating a difluorobenzene group resulted in slight blue shifts of 19 nm for the absorption peak and 15 nm for the emission peak in IR61-BF, which occurred at 779 nm (with an absorption coefficient of 1.604 × 10^5 M^{-1} cm^{-1}) and 800 nm, respectively. Notably, the emission spectrum of IR61-BF overlaps with the absorption spectrum of Nd^{3+} under an 808 nm laser, facilitating energy transfer from IR61-BF to UCNPs. It is important to note that IR61-BF exhibits a better overlap with Nd^{3+} absorption compared to IR61 (Fig. 1c and d), indicating a more efficient energy transfer to UCNPs. IR61-BF demonstrates an impressive fluorescence quantum yield of 24.9%, which is more than three times that of IR61, 8.1%.

3.2. Spectral properties of UCNPs

The core–shell structured NaYF$_4$:20%Yb0.5%Tm@NaYF$_4$:10%Yb20%Nd was synthesized using a solvothermal method. Initially, the NaYF$_4$:YbTm core provides blue light emission in the nanomaterials. Following this, NaYF$_4$:YbTm@NaYF$_4$:YbNd nanocrystals were produced through a seed-mediated shell growth strategy to enable excitation with 808 nm NIR light (Fig. 2a). Transmission electron microscopy (TEM) images (Fig. 2b) and dynamic light scattering (DLS) tests reveal that the average diameter of the core is 43.2 nm, while the diameter of the coated nanoparticles increases to 52.0 nm (Fig. S1). This core–shell design not only enhanced the energy transfer but also mitigated surface-related quenching of the UCL in the core. The crystal structure was also characterized by X-ray diffraction (XRD), and the synthesis of β-NaYF$_4$ was confirmed

 This journal is © The Royal Society of Chemistry 2025

Open Access Article. Published on 29 October 2025. Downloaded on 6/21/2026 12:21:52 PM.
This article is licensed under a Creative Commons Attribution-NonCommercial 3.0 Unported Licence.

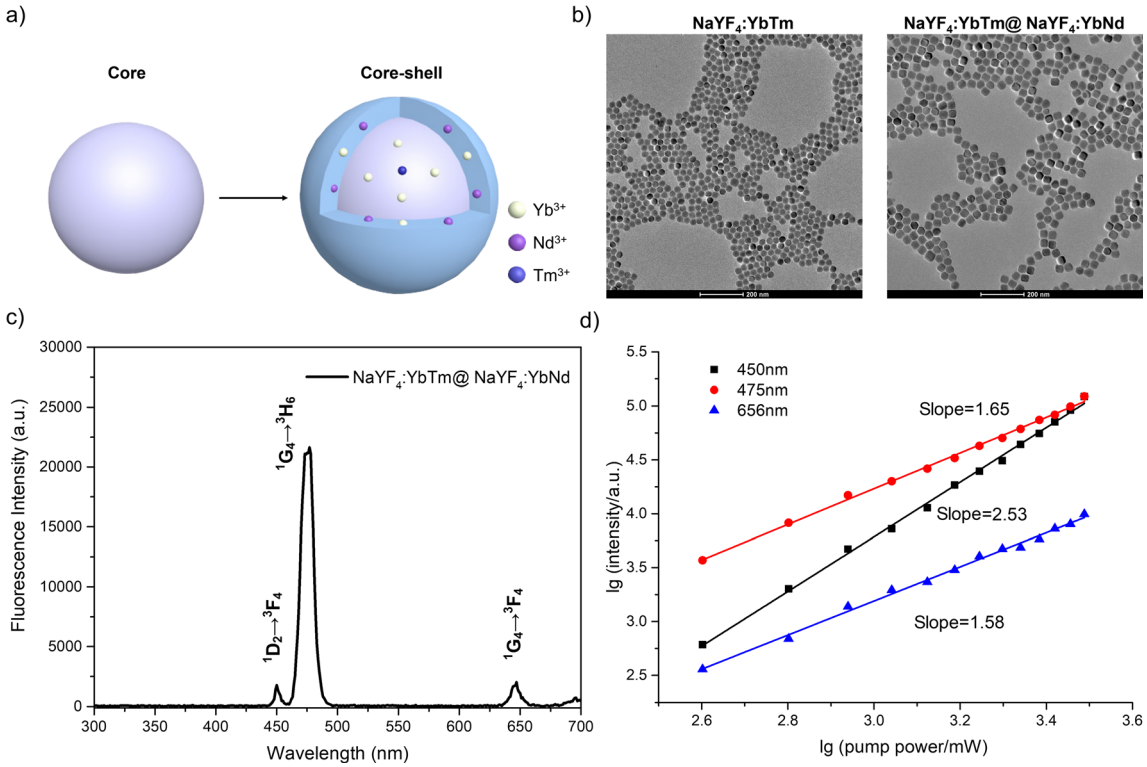

Fig. 2 (a) Schematic illustration of $NaYF_4$:YbTm and $NaYF_4$:YbTm@$NaYF_4$:YbNd UCNPs; (b) TEM images of UCNPs; (c) emission spectrum of $NaYF_4$:YbTm@$NaYF_4$:YbNd under 808 nm laser excitation (1 mg mL^{-1} in cyclohexane, laser: 2.8 W cm^{-2}, slit: 0.5 nm); and (d) intensity dependence of upconversion luminescence on the pump power in $NaYF_4$:YbTm@$NaYF_4$:YbNd.

according to the diffraction peak position and the standard JCPDS no. 28-1192 peak spectrum (Fig. S2).

As illustrated in Fig. 2c, the emission spectrum of $NaYF_4$:YbTm@$NaYF_4$:YbNd was obtained under 808 nm laser excitation. Without sensitizers, $NaYF_4$:YbTm was unable to absorb the excitation light at 808 nm, leading to a lack of upconversion emission. However, by incorporating an active shell around the core particle, blue light emission was achieved. Three distinct luminescence peaks were observed at 450 nm, 475 nm, and 646 nm, corresponding to the transitions $^1D_2 \rightarrow {}^3F_4$, $^1G_4 \rightarrow {}^3H_6$, and $^1G_4 \rightarrow {}^3F_4$ of Tm^{3+} ions, respectively.

As previously reported,[32] the relationship between the logarithm of pump power and the logarithm of upconversion intensity can be roughly expressed as $I_{out} \propto (I_{exc})^n$, where n represents the number of infrared photons absorbed to emit a visible photon. In this context, I_{out} is the output intensity and I_{exc} is the infrared excitation intensity. When plotted on a double-logarithmic scale, the slope of the I_{out}–I_{exc} curve indicates the value of n. From Fig. 2d, it can be inferred that the fluorescence emissions from UCNPs at 475 nm and 656 nm are associated with a two-photon process, whereas the emission at 450 nm corresponds to a three-photon process. The two-photon process is easier to implement than the three-photon process because the two-photon process requires fewer photons, a shorter energy transfer path, higher absorption efficiency, and less non-radiative loss.

3.3. Spectral properties of dye sensitized UCNPs

The overlap between the emission spectrum of dyes and the absorption spectrum of UCNPs is crucial for enhancing the energy transfer efficiency in dye-sensitized UCNP nanosystems. This spectral overlap enables efficient energy transfer, leading to an improved performance sensitization effect. By incorporating a difluorobenzene group into the structure of IR61, we developed a novel dye, IR61-BF, aimed at increasing the photosensitivity of UCNPs. The results indicate that the emission spectrum of IR61-BF, when excited with an 808 nm laser, closely aligns with the absorption spectrum of Nd^{3+} at 800 nm (Fig. 1d). This spectral matching is a crucial factor contributing to the higher sensitization effect of IR61-BF compared to IR61 on UCNPs.

Fig. S3 presents the FT-IR spectra of IR61-BF, OA-UCNPs, and NOBF-treated UCNPs. The band observed between 1600 and 1450 cm^{-1} in the IR spectrum of IR61-BF is attributed to the stretching vibration of the benzene skeleton within the molecule, while the band in the range of 910 to 665 cm^{-1} corresponds to the out-of-plane bending vibration of –CH in the benzene ring. Additionally, the C–F stretching vibration peak of the difluorobenzene group appears between 1300 and 1100 cm^{-1}. For the prepared OA-UCNPs, strong transmission bands at 2923 cm^{-1} and 2856 cm^{-1} are associated with the asymmetric and symmetric stretching vibrations of methylene

Open Access Article. Published on 29 October 2025. Downloaded on 6/21/2026 12:21:52 PM.
This article is licensed under a Creative Commons Attribution-NonCommercial 3.0 Unported Licence.

($-CH_2-$), respectively. The bands at 1557 cm^{-1} and 1465 cm^{-1} are linked to the vibrations of the carboxyl group. Following the treatment with $NOBF_4$, there was a noticeable reduction in the C–H stretching vibration intensity of OA molecules in the range of 2800 to 3000 cm^{-1}, as well as a decrease in the vibration peak of the carboxyl group (1600–1350 cm^{-1}). In contrast, the B–F stretching vibration peak (1100–1200 cm^{-1}) serves as a characteristic indication of the presence of tetrafluoroborate, confirming the successful exchange of $NOBF_4$ with the OA ligands on the surface of the prepared UCNPs.

To evaluate the sensitization effect of the dyes on UCNPs, we analyzed the upconversion emission spectra of IR61 and IR61-BF sensitized UCNPs. Initially, we used $NOBF_4$ to remove the oleic acid ligand from the surface of the UCNPs, followed by successfully grafting the dye onto the UCNP surface *via* the carboxyl side chain. Fig. 3a and b illustrate the energy transfer process from the dye to the UCNPs: the multiphoton upconversion process begins by absorbing NIR light energy and subsequently transferring that energy to Nd^{3+} ions within the UCNPs. Upon laser excitation at 808 nm, the hybrid UCNPs exhibit the characteristic upconversion emission enhancement of Tm^{3+}, with two emission peaks at 450 nm and 475 nm, respectively.

The regulation of UCL in Tm^{3+}-doped UCNPs is fundamentally rooted in the probabilistic quantum process of energy transfer upconversion (ETU), adhering to the principle of "lower-order priority over higher-order".[33] In this context, the 475 nm emission ($^1G_4 \rightarrow {}^3H_6$) corresponds to the lower-order ETU3 process, requiring two energy transfers, while the 450 nm emission ($^1D_2 \rightarrow {}^3F_4$) is associated with the higher-order ETU4 process, necessitating three energy transfers (Fig. 3b). Under low excitation conditions, characterized by

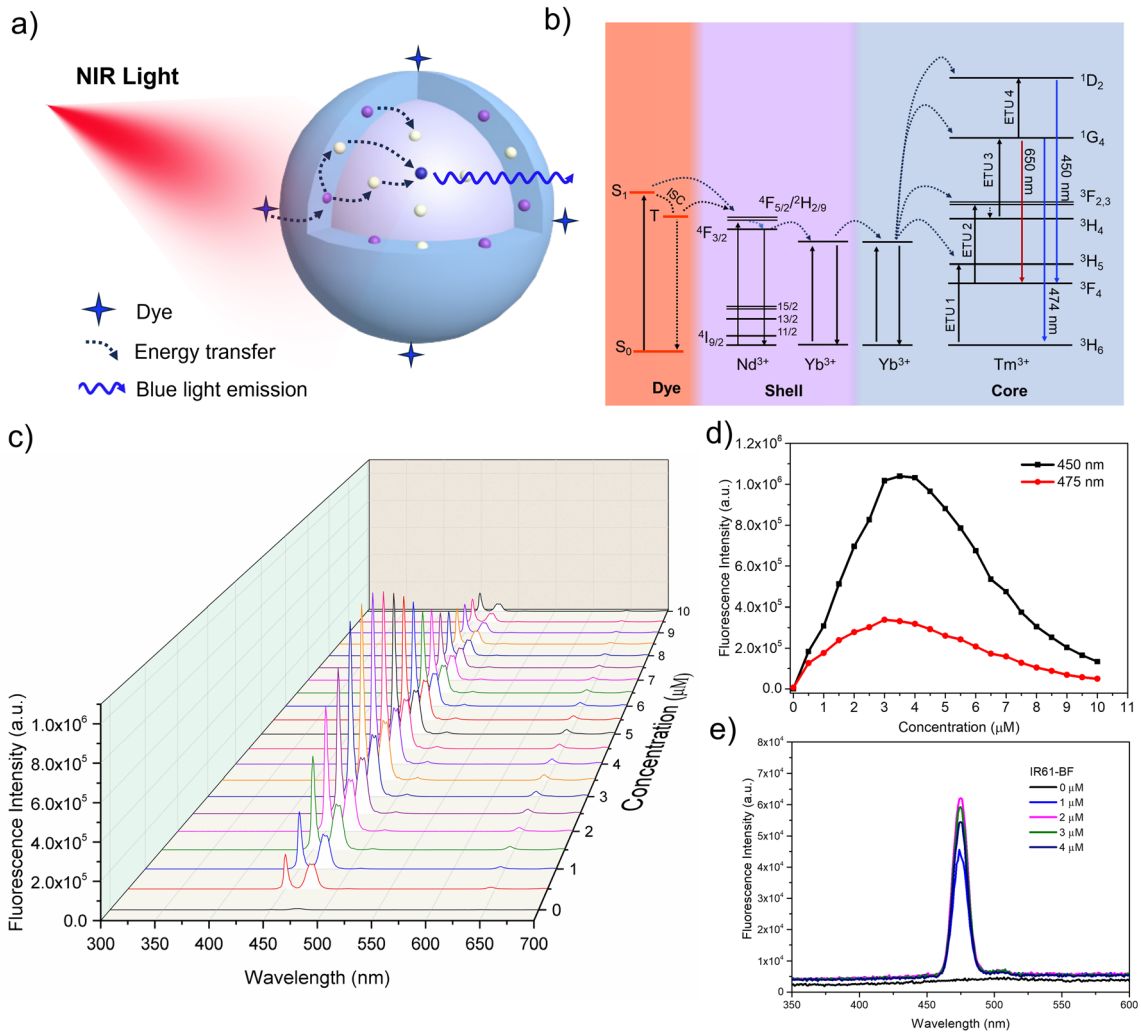

Fig. 3 (a) Schematic diagram of the dye-sensitized UCNP strategy and energy transfer. (b) Energy diagram of the upconversion mechanism in UCNPs and transition in Tm^{3+} ions yielding UV-blue emission. (c) Upconversion spectra of UCNPs with IR61-BF for sensitization in DMF excited at 808 nm (IR61-BF: 35 μM, 859.1-fold at 450 nm, 49.9-fold at 475 nm; UCNP: 1 mg mL^{-1} in DMF, laser: 2.8 W cm^{-2}, slit: 0.5 nm). (d) The upconversion emission intensity at 450 nm and 475 nm of dye-sensitized UCNPs as a function of dye concentration. (e) Upconversion spectra of IR61-BF sensitized-UCNPs in DMF excited using an 805 nm LED.

This journal is © The Royal Society of Chemistry 2025

Open Access Article. Published on 29 October 2025. Downloaded on 6/21/2026 12:21:52 PM.
This article is licensed under a Creative Commons Attribution-NonCommercial 3.0 Unported Licence.

low-power light or low dye concentration, the energy input is insufficient. As a result, ETU3 dominates, and the $^1G_4$ energy level does not reach saturation, leading to a predominance of the 475 nm emission. Conversely, under high excitation conditions, the $^1G_4$ energy level gradually approaches saturation. In this scenario, ETU3 increases slowly, while the excess energy shifts to ETU4. Additionally, a high concentration of dye significantly boosts the likelihood of Tm^{3+} receiving three energy transfers, propelling the population of the $^1D_2$ energy level into a phase of rapid growth. Consequently, the 450 nm emission surpasses the 475 nm emission, with a much greater increase observed (the UCL intensity is proportional to the concentration of excited-state electrons). The IR61-BF dye plays a crucial role in enhancing the UCL by markedly improving the energy absorption efficiency of UCNPs at the excitation wavelength.[34] The fluorescence spectrum data reveal that IR61-BF significantly enhances the fluorescence intensity of the UCNPs, resulting in brightness increases of 859.1-fold at 450 nm and 49.9-fold at 475 nm (Fig. 3c and d), particularly amplifying the three-photon upconversion process of the UCNPs. In contrast, the sensitization effect of the dye IR61 on the UCNPs is less pronounced compared to IR61-BF, which can be attributed to the higher quantum yield of IR61-BF and the superior overlap of its emission spectrum with the absorption spectrum of the UCNPs (Fig. S4). Additionally, we measured the fluorescence decay of the IR61-BF-sensitized UCNPs at both 450 nm and 475 nm (Fig. S5). The lifetime of the UCNPs sensitized with IR61-BF in the $^1D_2$ excited state is 316 μs, while the $^1G_4$ excited state decays slightly more slowly, with a lifetime of 426 μs. For hybrid UCNPs utilizing IR61 as the sensitizer, the lifetimes were also measured at 450 nm (372 μs) and 475 nm (418 μs). The sensitizing effect and lifetime regulation of IR61 and IR61-BF on UCNPs exhibit dependence on the emission wavelength. This phenomenon is attributed to the inherent characteristics of the lanthanide ion energy levels, including the influence of non-radiative transition probabilities and the upper limit of excited state filling. It is worth noting that IR61-BF exhibits a significant enhancement effect and strong energy transfer efficiency at 450 nm, as well as more pronounced lifetime changes at this specific wavelength. All of these provide direct photophysical evidence for the wavelength-dependent efficiency of the dye sensitization.

Further investigations revealed that the dye-sensitized UCNP system also demonstrated good luminescence performance when exposed to a low-power LED light source. The peak emission observed at 475 nm under LED excitation, as illustrated in Fig. 3e, highlights the potential use of the nanosystem in environments that require low-power light sources. It is worth noting that the optimal ratios of the dyes and UCNPs under LED or laser excitation are different, which stems from the ACQ effect of dyes (IR61-BF) (Fig. S6). The LED emits light through electroluminescence, with a wide wavelength range. This characteristic enables the LED to have a high matching degree with the absorption spectrum of the dye molecule IR61-BF and can efficiently excite its electronic transition. The molecule can be rapidly excited to a high energy state, resulting in a rapid increase in the density of excited-state molecules, intensifying the energy transfer and non-radiative recombination between molecules, and exhibiting a stronger ACQ effect. This study emphasizes the effectiveness of IR61-BF in enhancing the photosensitization performance of UCNPs, especially in applications that operate under low-power illumination.

UCNPs are typically synthesized in organic solvents, resulting in hydrophobic surfaces (UCNP@OA) that make direct dispersion in aqueous phases challenging. However, most biological applications require an aqueous environment. The amphiphilic DSPE-PEG molecule features a DSPE component (lecithin) that interacts with the hydrophobic regions of UCNPs, while the PEG (polyethylene glycol) segment enhances their dispersion in water. Furthermore, unmodified UCNPs may pose toxicity risks to biological systems. Encapsulating UCNPs with DSPE-PEG improves their water solubility and biocompatibility. The FT-IR spectra of DSPE-PEG coated UCNPs (UCNP@PEG) and the UCNP@PEG&IR61-BF products were analyzed in a similar manner. The UCNPs coated with DSPE-PEG exhibited a prominent characteristic peak for PEG in the range of 1000 to 1180 cm^{-1}, while an infrared peak corresponding to the phosphatidylethanolamine moiety was identified between 1050 and 1250 cm^{-1}. Additionally, subsequent processing confirmed the successful loading of the IR61-BF dye into UCNP@PEG (Fig. S7). By enveloping UCNPs with DSPE-PEG and incorporating IR61-BF into their shared hydrophobic segment, we significantly boosted the upconversion fluorescence emission (167.1-fold at 450 nm, 7.3-fold at 475 nm) (Fig. 4 and Fig. S8), thereby broadening their potential for biological applications and providing the possibility for low-power excitation. IR61-BF also showed a better sensitization effect than IR61, with a 99.3-fold fluorescence enhancement at 450 nm and a 5.6-fold fluorescence enhancement at 475 nm (Fig. S9).

3.4. Neuronal imaging with UCNPBF

Dye-sensitized UCNPs exhibit enhanced NIR absorption efficiency and increased UCL intensity compared to free UCNPs. This improvement significantly boosts imaging sensitivity and the signal-to-noise ratio. Additionally, dye sensitization allows for a broader range of excitation wavelengths, facilitating multi-color and multi-channel imaging, thereby greatly broadening the scope of applications in neuronal imaging. We selected the most effective luminescence combination of UCNP@PEG and 3 μM IR61-BF to develop the nanoprobe (UCNPBF), and to validate its feasibility for neuronal imaging, we conducted UCNPBF uptake experiments using C6 glioma cells. The neuronal uptake of the nanoprobe was assessed through confocal imaging after a 4-hour incubation with 200 μg mL^{-1} UCNPBF in C6 cells (Fig. 5). Additionally, we evaluated the biocompatibility of the probe using Neuro2a and NSC34 cells. As illustrated in Fig. S10, over 90% cell viability was recorded in both Neuro2a and NSC34 cells after 24 hours of incubation with varying concentrations (0–600 μg mL^{-1}) of

Open Access Article. Published on 29 October 2025. Downloaded on 6/21/2026 12:21:52 PM.
This article is licensed under a Creative Commons Attribution-NonCommercial 3.0 Unported Licence.

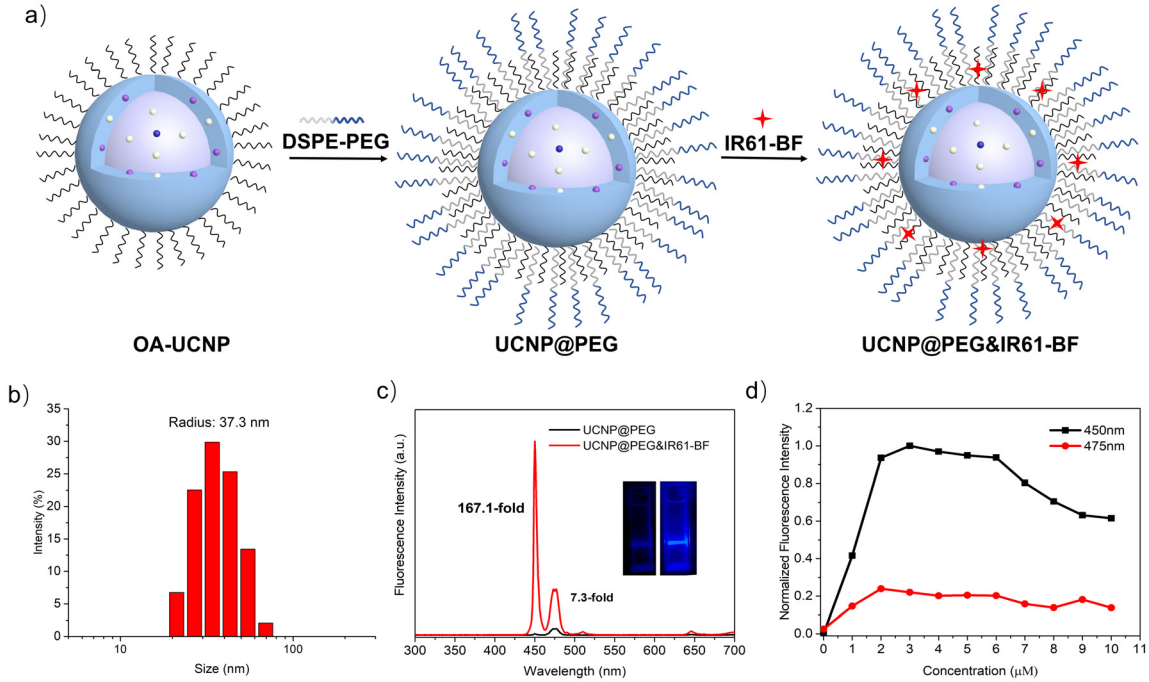

Fig. 4 (a) Schematic diagram of UCNP surface modification and dye sensitization. (b) DLS data of UCNP@PEG. (c) Upconversion spectra of UCNP@PEG and UCNP@PEG&IR61-BF (1 mg mL^{-1}, IR61-BF: 3 μM) under 808 nm laser irradiation in aqueous solution (laser: 2.8 W cm^{-2}); inset: photographs of the UCL of UCNP@PEG (left) and UCNP@PEG&IR61-BF (right) under an 808 nm laser (50 mW). (d) The upconversion emission intensity at 450 nm and 475 nm of dye-sensitized UCNP@PEG as a function of dye concentration (UCNP@PEG: 1 mg mL^{-1}, IR61-BF: 0–10 μM, laser: 2.8 W cm^{-2}, slit: 1 nm, water solution).

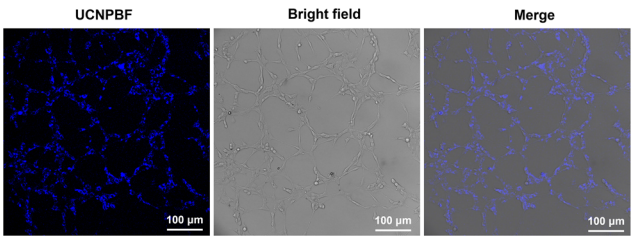

Fig. 5 The confocal imaging of C6 cells was performed after treatment with 200 μg mL^{-1} UCNPBF for 4 hours (808 nm laser).

UCNPBF in the culture medium, demonstrating its excellent biocompatibility.

Axonal transport is a bidirectional process in which proteins, organelles, and signaling molecules are actively moved along microtubule tracks within neurons.[35,36] This process is essential for maintaining neuronal polarity, supporting synaptic function, and preserving the integrity of neural circuits.[37] Traditionally, it has been thought that anterograde transport, which moves unidirectionally from the soma to the axon terminal and is mediated by kinesin motor proteins, predominates in axonal transport. However, recent studies have demonstrated that retrograde transport, driven by dynein motor proteins, also plays a vital role.[38–40] It not only contributes to the feedback signaling of neurotrophic factors, such as brain derived neurotrophic factor (BDNF) and nerve growth factor (NGF), back to the soma, but also facilitates trans-synaptic regulation from the postsynaptic to presynaptic site through retrograde signaling molecules like endocannabinoids and nitric oxide.[41,42] This retrograde transport system underpins the dynamic regulation of neural plasticity and circuit homeostasis. Its dysfunction is closely associated with various neurodegenerative diseases, neurodevelopmental disorders, and infectious diseases. For example, in Alzheimer's disease, impaired retrograde axonal transport results in autophagy disorders.[43–45] Furthermore, in early stages of amyotrophic lateral sclerosis (ALS) and other related conditions, axonal damage characterized by degradation and swelling has been observed in both the ventral root (VR) and dorsal root (DR).[46–48] To investigate the molecular mechanisms of retrograde transport, this study utilized a microfluidic chamber to establish a primary neuron culture model, confirming the retrograde delivery efficiency of UCNPBF nanoparticles through a spatiotemporally controllable microenvironment design. This system provides a novel experimental framework for clarifying the pathological mechanisms associated with neurological diseases.

Fig. 6a and b illustrate the schematic diagram of the process for culturing primary cortical neurons in the microfluidic device. This device consists of two chambers, connected by a 500 μm-long microchannel. To establish the neuronal microfluidic model, we isolated fresh cortical neurons from mouse embryos and verified them by Tuj1 (Fig. S11), and then cul-

This journal is © The Royal Society of Chemistry 2025

Open Access Article. Published on 29 October 2025. Downloaded on 6/21/2026 12:21:52 PM.
This article is licensed under a Creative Commons Attribution-NonCommercial 3.0 Unported Licence.

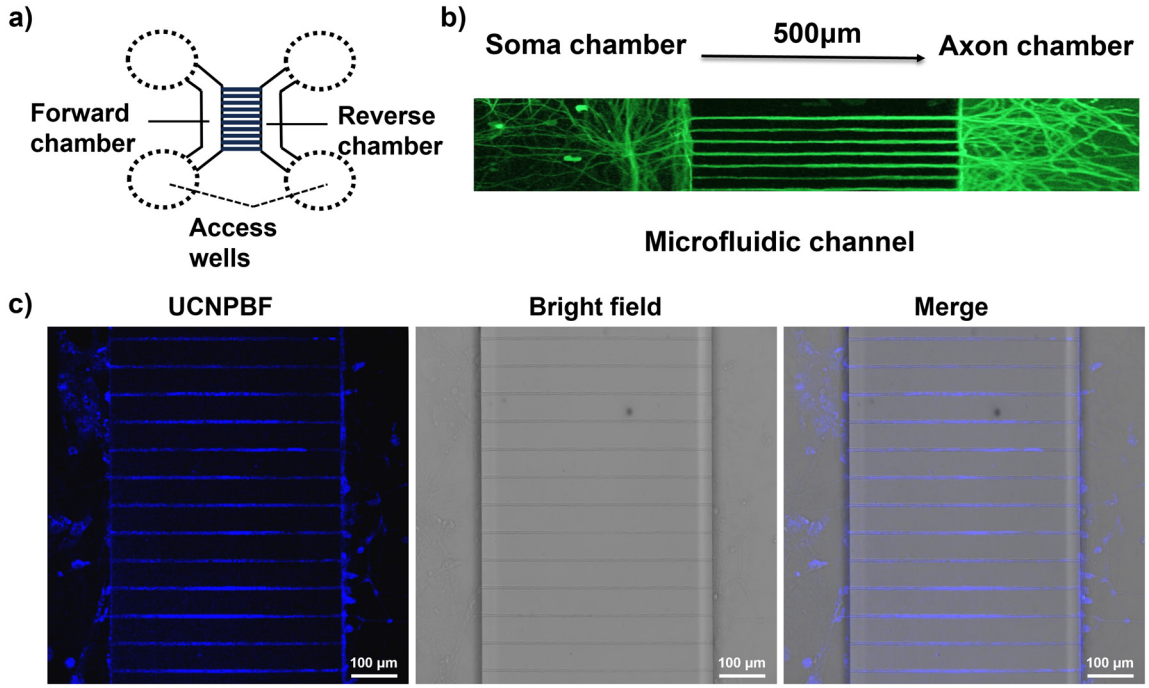

Fig. 6 (a) Schematic of the microfluidic chambers. (b) Confocal image of the cortical neuron axons extending fully into the right chamber (axon side). (c) Confocal image of primary cortical neurons in the microfluidic device after 24 h incubation with UCNPBF (0.2 g mL^{-1}) at the axon chamber.

tured them in the soma chamber (left), allowing the axons to grow through the microchannel to the axon chamber (right) within 10 days (Fig. 6b). Next, UCNPBF was added to the axon chamber. By maintaining a 50 μL volume difference between the axonal and soma compartments using liquid resistance microchannels, we ensured that all transport events and the accumulation of the UCNPs in the soma chamber were solely due to axonal transport from the axonal compartment. Fig. 6c illustrates the fluorescence confocal imaging of primary cortical neurons that were incubated for 24 hours with only the axon chamber containing UCNPBF. UCNPBF particles were observed within axons of primary neurons and subsequently detected in the soma chamber, indicating successful retrograde transport. This finding can be attributed to the retrograde transport of nanomaterials along the axons.

Our results demonstrate a significant increase in performance through systematic modification of the heptamethine cyanine framework, and a new type of NIR dye, IR61-BF, has been synthesized. Specifically, the introduction of a benzoic acid side chain helps to anchor UCNPs, while reducing the interfacial distance between the dye and the surface sensitizers (Nd^{3+}) of the nanoparticles, thus enhancing the interaction between the dye and the lanthanide ions. In conventional heptamethine cyanine structures, the chlorine (–Cl) atom is frequently substituted with various functional groups to modulate spectroscopic properties. However, achieving suitable spectral characteristics and high quantum yields has proved challenging. In our study, a difluorophenyl group was strategically employed to replace the chloride atom, serving as an electron acceptor and modifying the conjugated structure of the dye. This substitution resulted in a suitable blue shift in both absorption and emission wavelengths, alongside noticeable increases in absorption coefficient and fluorescence quantum yield. The presence of two highly electronegative fluorine atoms facilitated a balance between spectral characteristics and quantum yield, thus positioning IR61-BF as an ideal candidate for enhancing UCNP sensitivity.

Following the first point, the second concept is that core–shell structured UCNPs ($NaYF_4$:YbTm@$NaYF_4$:YbNd) were selected to achieve blue light emission, leveraging the distinct advantages associated with this architecture in energy transfer efficiency and minimization of energy loss. The incorporation of Nd^{3+} ions within the active shell layer significantly increased the UCNPs' ability to absorb NIR light at 808 nm, thereby providing an abundance of excitation energy essential for the energy transfer mechanisms. The spatial distribution of Nd^{3+} and Tm^{3+} ions across disparate shell layers effectively mitigated cross-relaxation phenomena, thereby reducing superfluous energy loss and enhancing the overall efficiency of energy migration. Additionally, Yb^{3+} ions present in the core and shell layer functioned as pivotal intermediaries, facilitating energy transfer from Nd^{3+} to Yb^{3+}, and subsequently from Yb^{3+} to Tm^{3+}.

Spectral analysis indicated a robust congruence between the emission spectrum of IR61-BF and the absorption spectrum of Nd-doped UCNPs, thereby reinforcing the framework for efficient energy transfer. By combining IR61-BF with UCNPs, we delivered a dye-sensitized nanosystem; fluorescence

Open Access Article. Published on 29 October 2025. Downloaded on 6/21/2026 12:21:52 PM. This article is licensed under a Creative Commons Attribution-NonCommercial 3.0 Unported Licence.

titration assays revealed an extraordinary enhancement in upconversion emission intensity, with an increase of 859.1-fold in IR61-BF sensitized UCNPs relative to their unsensitized counterparts. This substantial enhancement underscores the exceptional sensitizing efficacy of IR61-BF on UCNPs. Furthermore, the encapsulation of hydrophobic UCNPs within the amphiphilic DSPE-PEG ligand, along with the incorporation of IR61-BF into their hydrophobic regions, facilitated successful sensitization in aqueous environments, achieving a fluorescence enhancement of 167.1-fold. This output not only surpasses the majority of previously reported NIR dyes but also substantiates the system's stability and prospective biomedical applications.

By leveraging the pronounced sensitization attributes of IR61-BF, we constructed the nanoprobe UCNPBF, which could serve better in neuronal imaging applications. We demonstrated that through optimization of the dye and UCNP concentration, an excellent high sensitization effect could be achieved. Initial experiments verified the uptake capabilities of UCNPBF in C6 glioma cells, followed by the establishment of a cortical neuron microfluidic model to evaluate neuronal retrograde transport properties. The results demonstrated successful neuronal uptake and retrograde transport of UCNPBF, highlighting its potential applicability in neuronal imaging and studying the axonal retrograde transport mechanisms.

4. Conclusion

In conclusion, a new type of NIR dye, IR61-BF, was synthesised and it achieved efficient fluorescence enhancement of UCNPs in organic solutions and demonstrated outstanding sensitization performance in aqueous solutions. This provides new methods for the development of high-performance fluorescent probes. Moreover, the nanoprobe UCNPBF constructed based on IR61-BF sensitized UCNPs shows broad application prospects in neuronal imaging and neuronal retrograde transport tracking. Future research can explore the application of this nanoprobe in other biomedical fields and neuroscience fields.

Author contributions

Angelo All (AA) contributed to the conception and experimental design. Hengde Li (Hli) performed material synthesis, characterization, data analysis, and drafted the paper. Hli and Haitao Liu (HL) performed literature search. AA, Ka-Leung Wong (K.-L. Wong), and Mohsen Adeli (MA) provided critical revisions. All authors collaborated and contributed to the project. All authors have read and agreed to the published version of the manuscript.

Conflicts of interest

All authors declare that they have no conflicts of interest.

Data availability

The data supporting this article have been included as part of the supplementary information (SI). Supplementary information is available. Details of material synthesis and characterization (DLS data, XRD, FT-IR, NMR spectroscopy, and mass spectrometry), experimental methods, supporting figures, dye/UCNP ratio, MTT test, and characterization of cortical neurons. See DOI: https://doi.org/10.1039/d5nr03288a.

Acknowledgements

This study was partially supported by: 2021–22 General Research Fund of Hong Kong (Project Number: 12100121), and 2025–26 General Research Fund of Hong Kong (Project Number: 12301225), and 2020-21 Hong Kong Baptist University: Initiation Grant for Faculty Niche Research Areas (Project Number: RC-FNRA-IG/20-21/SCI/02). The authors wish to thank Prof. Ka-Leung Wong's students at the Hong Kong Polytechnic University for their invaluable contributions in experimental procedures. The authors also want to thank the wonderful support staff from the Chemistry Department at Hong Kong Baptist University for all their contributions to our experimental work. The authors truly appreciate everyone's support.

References

1 F. Wang and X. Liu, *Chem. Soc. Rev.*, 2009, **38**, 976–989.
2 H. Li, H. Liu, K.-L. Wong and A. All, *Biomater. Sci.*, 2024, **12**, 4650–4663.
3 S. Zha, H. Li, G.-L. Law, K.-L. Wong and A. H. All, *Mater. Des.*, 2023, **227**, 111800.
4 Y. Lin, Y. Yao, W. Zhang, Q. Fang, L. Zhang, Y. Zhang and Y. Xu, *Acta Biomater.*, 2021, **135**, 1–12.
5 J. Lin, B. Xing and D. Jin, *Adv. Opt. Mater.*, 2023, **11**, 2300802.
6 D. W. Kim, P. Wrede, A. Rodríguez-Camargo, Y. Chen, N. O. Dogan, C. Glück, B. V. Lotsch, D. Razansky and M. Sitti, *Adv. Mater.*, 2025, 2418425.
7 Z. Yi, A. H. All and X. Liu, *Optogenetics: Light-Sensing Proteins and Their Applications in Neuroscience and Beyond*, 2021, pp. 641–657.
8 Y. Li, B. Yang, Y. Wang, Z. Huang, J. Wang, X. Pu, J. Wen, Q. Ao, K. Xiao and J. Wu, *Nano Lett.*, 2024, **24**, 5403–5412.
9 X. Zeng, S. Chen, A. Weitemier, S. Han, A. Blasiak, A. Prasad, K. Zheng, Z. Yi, B. Luo and I. H. Yang, *Angew. Chem.*, 2019, **131**, 9363–9369.
10 H. Li, S. Zha, H. Li, H. Liu, K. L. Wong and A. H. All, *Small*, 2022, **18**, 2203629.
11 J. Zeng, Y. Shang, S. Hao, T. Chen, Z. Sun, H. Liu and C. Yang, *Mater. Today Phys.*, 2024, 101520.
12 L. Liang, X. Qin, K. Zheng and X. Liu, *Acc. Chem. Res.*, 2018, **52**, 228–236.

This journal is © The Royal Society of Chemistry 2025

Open Access Article. Published on 29 October 2025. Downloaded on 6/21/2026 12:21:52 PM. This article is licensed under a Creative Commons Attribution-NonCommercial 3.0 Unported Licence.

13 X. Fu, S. Fu, Q. Lu, J. Zhang, P. Wan, J. Liu, Y. Zhang, C.-H. Chen, W. Li and H. Wang, *Nat. Commun.*, 2022, **13**, 4741.
14 C. Zhai, G. Liu, X. Xie, J. Gao and Y. Ma, *Chem. Mater.*, 2025, **37**, 1468–1477.
15 X. Meng, T. Shen, W. Zhang, R. Luo, J. Zhou, R. Liao, R. Zhao and C. Cao, *ACS Appl. Mater. Interfaces*, 2025, **17**, 8191–8197.
16 J. Wang, Y. Yang, A. A. Aryee, N. Wang and Z. Li, *Food Control*, 2024, **165**, 110680.
17 G. Bao, R. Deng, D. Jin and X. Liu, *Nat. Rev. Mater.*, 2025, **10**, 28–43.
18 J. Ke, S. Lu, Z. Li, X. Shang, X. Li, R. Li, D. Tu, Z. Chen and X. Chen, *Nano Res.*, 2020, **13**, 1955–1961.
19 M. Xu, Y. Lin, Y. Li, Y. Dong, C. Guo, X. Zhou and L. Wang, *Small*, 2024, **20**, 2406879.
20 X. Wang, R. R. Valiev, T. Y. Ohulchanskyy, H. Ågren, C. Yang and G. Chen, *Chem. Soc. Rev.*, 2017, **46**, 4150–4167.
21 X. Liu, T. Liu, Y. Feng and C.-J. Yao, *ACS Appl. Opt. Mater.*, 2023, **2**, 1733–1750.
22 Z.-Q. Liang, Z.-Y. Zou, X. Yan, X.-B. Zhang, D.-D. Song, C.-Q. Ye, X.-M. Wang and X.-T. Tao, *J. Mater. Chem. C*, 2022, **10**, 2205–2212.
23 J.-P. Goddard, N. Sellet, J. Frey and M. Cormier, *Chem. Sci.*, 2024, **15**, 8639–8650.
24 G. Bao, S. Wen, W. Wang, J. Zhou, S. Zha, Y. Liu, K.-L. Wong and D. Jin, *Nano Lett.*, 2021, **21**, 9862–9868.
25 X. Zhao, Z. Fan, Y. Qiao, Y. Chen, S. Wang, X. Yue, T. Shen, W. Liu, J. Yang and H. Gao, *ACS Appl. Mater. Interfaces*, 2020, **12**, 16114–16124.
26 Y. Liu, L. Ning, Y. Luo, Y. Huang, Z. He, H. Ma, Y. Zhao, J. Zhang, D. Liu and L. Fu, *Nano Lett.*, 2024, **24**, 12486–12492.
27 J. Hu, B. Zhao, R. Wen, X. Zhang, Y. Zhang, D. S. Kohane and Q. Liu, *Nano Lett.*, 2023, **23**, 5209–5216.
28 H. Liu, A. Kulkarni, U. Kostiv, E. Sandberg, A. Lakshmanan, G. A. Sotiriou and J. Widengren, *Adv. Opt. Mater.*, 2024, **12**, 2400987.
29 S. Chen, J. Wu, A. Cai, N. Gonzalez and R. Yin, *Neurosci. Res.*, 2020, **152**, 59–65.
30 F. Zhao, J. Hu, D. Guan, J. Liu, X. Zhang, H. Ling, Y. Zhang and Q. Liu, *Adv. Mater.*, 2023, **35**, 2304907.
31 T. Liang, Q. Wang, Z. Li, P. Wang, J. Wu, M. Zuo and Z. Liu, *Adv. Funct. Mater.*, 2020, **30**, 1910765.
32 Y. Kuisheng, L. Yan, Y. Chaoyi, L. Liping, Y. Chanhua and Z. Xiyan, *J. Rare Earths*, 2006, **24**, 757–760.
33 J. S. Matias, K. Komolibus, W. K. Kiang, S. Konugolu-Venkata-Sekar and S. Andersson-Engels, *Nanoscale*, 2024, **16**, 3641–3649.
34 G. Chen, J. Damasco, H. Qiu, W. Shao, T. Y. Ohulchanskyy, R. R. Valiev, X. Wu, G. Han, Y. Wang and C. Yang, *Nano Lett.*, 2015, **15**, 7400–7407.
35 Z. Han, N. Luo, W. Ma, X. Liu, Y. Cai, J. Kou, J. Wang, L. Li, S. Peng and Z. Xu, *Nat. Commun.*, 2023, **14**, 3792.
36 G.-J. Xiong and Z.-H. Sheng, *J. Cell Biol.*, 2024, **223**, e202401145.
37 E.-M. Krämer-Albers and H. B. Werner, *Nat. Rev. Neurosci.*, 2023, **24**, 474–486.
38 H. Zhao, L. Guillaud, M. F. Emily, X. Xu, L. Moshniaha, H. Hanayama, R. Kabe, M. Terenzio and A. Narita, *ACS Nano*, 2024, **18**, 34730–34740.
39 Y. Wang, S. Li, X. Liang, J. Fan, S. Li, F. Zhou, X. Li, M. Lai, D. Feng and Y. Li, *Alzheimer's Res. Ther.*, 2025, **17**, 132.
40 Z. Yi, A. H. All, Y. Liu and X. Liu, *ACS Nano*, 2025, **19**, 35306–35321.
41 M. Fogarty, O. Khurram, C. Mantilla and G. Sieck, *Physiology*, 2023, **38**, 5730028.
42 X. Wang, Y. Hu and R. Xu, *Neural Regener. Res.*, 2024, **19**, 800–806.
43 R. Meng, Y. Li, X. Yang, Y. Cheng, M. Xu, L. Zhou, C. Wu, S. Yu, W. Huang and T. Wang, *Adv. Mater.*, 2025, **37**, 2413614.
44 I. Raïch, J. Lillo, J. B. Rebassa, C. Griñán-Ferré, A. Bellver-Sanchis, I. Reyes-Resina, R. Franco, M. Pallàs and G. Navarro, *Alzheimer's Res. Ther.*, 2025, **17**, 109.
45 Z. Yi, A. H. All, Y. Liu and X. Liu, *ACS Nano*, 2025, **19**, 35306–35321.
46 T. Fan, J. Peng, H. Liang, W. Chen, J. Wang and R. Xu, *Neural Regener. Res.*, 2026, **21**, 972–988.
47 C. Alberti, F. Rizzo, A. Anastasia, G. Comi, S. Corti and E. Abati, *Neurobiol. Dis.*, 2024, **193**, 106467.
48 X. Chen, S. Lv, J. Liu, Y. Guan, C. Xu, X. Ma, M. Li, X. Bai, K. Liu and H. Zhang, *Cells*, 2024, **13**, 2076.